J. Comp. App. Res. Mech. Eng. Vol. 15. No. 2, pp. 209-231, 2026 *DOI: 10.22061/jcarme.2026.12648.2745*

Journal of Computational and Applied Research in Mechanical Engineering

jcarme.sru.ac.ir

SRTTU

JCARME

ISSN: 2228-7922

Research paper

Influence of friction stir welding parameters on microstructural evolution and mechanical behavior of AA6082-T6 aluminum alloy

Worapong Boonchouytan[a,b*], Watthanaphon Cheewawuttipong[a] and Prapas Muangjunburee[c]

[a]*Program in Production Engineering, Faculty of Engineering, Rajamangala University of Technology Srivijaya, Songkhla, 90000, Thailand*
[b]*Materials Processing Technology Research Unit, Faculty of Engineering, Rajamangala University of Technology Srivijaya, Songkhla, 90000, Thailand*
[c]*Department of Mining and Materials Engineering, Faculty of Engineering, Prince of Songkla, Songkhla, 90000, Thailand*

Article info:

Article history:

Received: 25/10/2025
Revised: 16/01/2026
Accepted: 19/01/2026
Online: 22/02/2026

Keywords:

Friction stir welding,
Aluminum alloy,
Dynamic recrystallization,
Mechanical behavior,
Microstructural evolution.

[*]Corresponding author:
worapong.b@rmutsv.ac.th

Abstract

This study investigates the effects of tool rotational speed and traverse speed on the microstructural development and mechanical characteristics of friction stir-welded AA6082-T6 aluminum alloy joints. Welding was performed at rotational speeds of 710, 1000, and 1400 rpm and traverse rates of 14, 28, and 56 mm/min to elucidate the correlation between process parameters, relative heat input, and joint performance. The macrostructural analysis verified the presence of robust weld production devoid of macroscopic flaws across all parameter combinations. Optical microscopy demonstrated polished equiaxed grains in the stir zone, indicative of deformation-induced recrystallization during solid-state processing, while the redistribution of Mg_2Si and Al_6Mn containing phases facilitated microstructural homogenization. Mechanical tests indicated that hardness and tensile strength typically rose with higher rotational and traverse rates, reaching peak values of 73.77 HV and 111.77 MPa at 1400 rpm and 56 mm/min, respectively. Impact toughness attained a peak value of 13.00 Nm at 1000 rpm and 14 mm/min, where modest heat input and strain rate facilitated a more ductile fracture behavior. The results suggest that joint behavior is determined by the equilibrium between temperature exposure and plastic deformation, rather than by a singular predominant factor. A balance between strength and impact toughness was achieved within the current parameter range of 1000–1400 rpm and 14–56 mm/min, offering practical guidelines for the optimization of AA6082-T6 friction stir welds.

1. Introduction

Friction stir welding (FSW) is widely recognized as an advanced solid-state joining technique, particularly suitable for aluminum alloys that are difficult to weld using conventional fusion-based processes. Since its introduction by The Welding Institute (TWI) in the early 1990s, FSW has demonstrated significant advantages in minimizing solidification-related defects such as

porosity, hot cracking, and excessive heat-affected zone (HAZ) softening by maintaining the material below its melting temperature during joining [1–3]. The process relies on frictional heat generation and severe plastic deformation induced by a rotating non-consumable tool, which promotes effective material mixing and microstructural refinement within the stir zone (SZ) [2, 4].

Among heat-treatable aluminum alloys, AA6082-T6 from the 6xxx series has attracted considerable attention due to its high strength-to-weight ratio, good corrosion resistance, and excellent formability, making it a preferred material for transportation, marine, and structural applications [5, 6]. However, conventional fusion welding of AA6082-T6 often results in degraded joint performance owing to porosity formation, hot cracking, and dissolution or coarsening of strengthening Mg_2Si precipitates within the HAZ [7]. These limitations have driven extensive research into the application of FSW as an alternative joining technique for this alloy system.

Previous studies have shown that FSW of AA6082-T6 produces a characteristic zonal microstructure consisting of the base metal (BM), HAZ, thermo-mechanically affected zone (TMAZ), and SZ, with the latter typically composed of fine equiaxed grains formed through dynamic recrystallization [8-11].

The face-centered cubic (FCC) crystal structure of aluminum facilitates dislocation motion, recovery, and recrystallization, enabling significant grain refinement under appropriate thermal–mechanical conditions [1]. Nevertheless, the asymmetric material flow between the advancing side (AS) and retreating side (RS), coupled with non-uniform temperature distribution, results in heterogeneous microstructural evolution and mechanical response across the weld region [9, 12].

Recent investigations have emphasized that tool rotational speed and traverse speed are the dominant parameters governing heat input in FSW joints of AA6082 and related 6xxx-series alloys [9]. These parameters directly control material flow behavior and precipitate evolution within the weld region. Moderate heat input promotes continuous dynamic recrystallization (CDRX) and uniform redistribution of Mg_2Si precipitates, leading to enhanced strength and hardness, whereas excessive heat input may induce precipitate coarsening and localized softening within the TMAZ and HAZ [11].

Conversely, insufficient heat input can result in incomplete plasticization and unstable material flow, compromising joint integrity [13, 14]. In addition, recent studies have significantly advanced the understanding of friction stir welding by emphasizing the coupled roles of heat input, strain rate, and tool kinematics in governing microstructural evolution and mechanical performance of aluminum alloys [15–17].

In particular, both experimental and analytical investigations have demonstrated that tool rotational speed and traverse speed jointly control the thermal cycle and plastic flow stability, thereby directly influencing grain refinement mechanisms, precipitate dissolution and reprecipitation behavior, and residual stress development [18–20].

Several recent works have highlighted that the existence of an optimized processing window is critical for achieving defect-free welds with a balanced combination of strength and ductility, especially in heat-treatable aluminum alloys used for structural and transportation applications [16, 19, 21].

Numerical simulations and coupled experimental studies further revealed that excessive heat input promotes precipitate coarsening and local softening in the thermo-mechanically affected regions, whereas insufficient heat input results in incomplete plasticization, unstable material flow, and reduced joint integrity [17, 18, 22].

Moreover, emerging research has stressed the importance of integrated process–structure–property approaches that combine microstructural characterization with mechanical testing to reliably predict joint performance and service behavior [20, 21].

Despite these advances, systematic experimental investigations focusing specifically on AA6082-T6 that simultaneously correlate welding

parameters, detailed microstructural evolution, and multiple mechanical properties, including hardness, tensile strength, and impact toughness, remain limited. This gap highlights the need for comprehensive studies conducted within well-defined thermal mechanical regimes to establish robust processing property relationships for this alloy system.

Although numerous studies have examined the friction stir welding of 6xxx-series aluminum alloys, most investigations have focused on individual mechanical properties such as hardness or tensile strength and have typically considered limited ranges of process parameters without establishing a comprehensive link to microstructural evolution. There is still relatively little research on AA6082-T6 that evaluates macrostructural characteristics, microstructural refinement in various weld zones, precipitate redistribution, and several mechanical responses, including tensile strength, hardness, and impact toughness within distinct process regimes.

The synergistic impact of elevated rotational speed and high traverse speed on concurrent changes in hardness and impact toughness has not been comprehensively elucidated. The current study seeks to establish a coherent process–structure–property relationship for friction stir-welded AA6082-T6 by (i) investigating microstructural alterations across the SZ–TMAZ–HAZ under varying thermal–mechanical conditions and (ii) correlating grain refinement and precipitate redistribution with properties related to strength and toughness. The outcomes aim to offer pragmatic direction for choosing FSW parameters based on specified joint performance criteria.

In this context, the present study systematically investigates the influence of tool rotational speed and traverse speed on the microstructural evolution and mechanical behavior of friction stir-welded AA6082-T6 joints. Welding parameters were selected to represent low, intermediate, and high heat-input regimes commonly reported in the literature, enabling a direct assessment of thermal–mechanical effects on grain refinement, precipitate redistribution, and joint performance. Unlike many previous studies, this work integrates macrostructural, microstructural, and mechanical properties, including hardness, tensile strength, and impact toughness, to provide a comprehensive understanding of process optimization for achieving an optimal balance between strength and ductility in FSW AA6082-T6 joints.

2. Experimental procedure

2.1. Preparation of the welding specimens

The AA6082-T6 aluminum alloy was chosen as the primary material owing to its excellent strength-to-weight ratio, commendable corrosion resistance, and exceptional weldability in solid-state joining scenarios. Table 1 presents the alloy's chemical composition, demonstrating that magnesium and silicon act as principal strengthening agents via precipitation hardening, whilst manganese facilitates grain refinement and enhances mechanical strength.

The plates were precisely cut to the required dimensions utilizing a CHENLONG horizontal band saw (Model CS-230) for low-heat sectioning and subsequently milled with a TOS Olomouc vertical milling machine (Model FGV 32) to achieve smooth and uniform surfaces. Each specimen was sized 25 mm × 100 mm × 6 mm, as depicted in Fig. 1. Before welding, all samples were cleaned with acetone to remove surface contaminants and prevent oxidation.

These preparatory measures guaranteed uniform testing settings and dependable assessment of weld quality across diverse process parameters.

2.2. Friction stir welding tool

The friction stir welding tool was manufactured using SKD11 tool steel, offering superior hardness, exceptional wear resistance, and sufficient thermal stability under FSW circumstances.

Table 1. Chemical composition of AA6082-T6 aluminum alloy (wt.%).

Element	Content (wt.%)
Si	0.7–1.3
Fe	≤0.5
Cu	≤0.1
Mn	0.4–1.0
Mg	0.6–1.2
Cr	≤0.25
Zn	≤0.2
Ti	≤0.1
Al	Balance

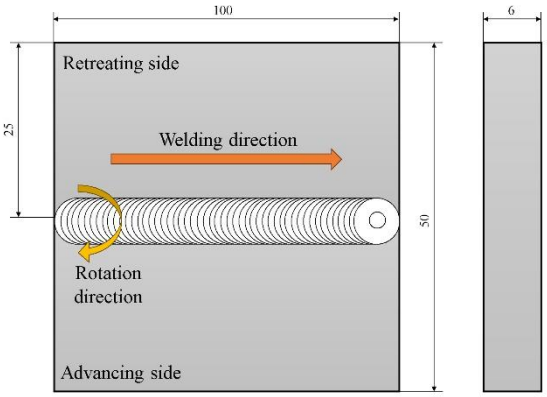


Fig. 1. Test specimen dimensions and butt joint configuration prepared for the friction stir welding process.

These attributes render SKD11 appropriate for welding aluminum alloys, especially within the current experimental parameter range.
The tool comprises three functional components: a flat cylindrical shoulder with a diameter of 15 mm, a threaded cylindrical pin with a diameter of 5 mm and a length of 4.8 mm, and a shank with a diameter of 20 mm for secure attachment to the machine spindle. Threaded cylindrical pins have been extensively documented to facilitate material flow and mixing during friction stir welding of 6xxx-series aluminum alloys, hence improving consolidation and joint formation.
The chosen material and tool geometry facilitated consistent stirring conditions during the welding experiments, guaranteeing reproducible weld quality. The comprehensive configuration of the tool is illustrated in Fig. 2.

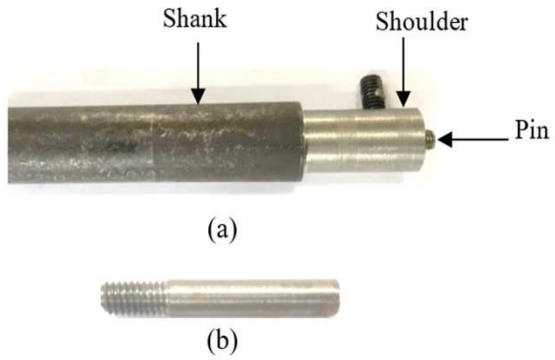


Fig. 2. Friction stir welding tool: (a) components of the welding tool, and (b) configuration of the threaded pin.

2.3. Workpiece clamping and supporting system

The AA6082-T6 aluminum alloy plates were securely clamped in a precision mechanical vise during welding to avert any movement or vibration that would jeopardize the integrity of the weld. A medium-carbon steel base plate was placed beneath the specimens to offer structural support and counteract the downward forging force applied by the spinning tool shoulder.
The backing plate was adjusted to the height of the vise base to guarantee consistent clamping pressure. A thermal insulation gasket was placed under the backing plate to reduce heat transfer from the welded sample to the milling machine table. This design safeguarded the equipment and ensured consistent thermal conditions during welding. Fig. 3 illustrates the complete clamping and support apparatus, comprising the vise, aluminum workpiece, steel backing plate, and insulating layer. Accurate alignment and secure attachment of all components were essential for ensuring consistent material flow and optimal weld performance.

2.4. FSW machine setup and process parameters

Friction stir welding studies were conducted with a modified vertical milling machine tailored for FSW, enabling meticulous regulation of tool rotational and traverse speeds. An SKD11 tool, which is non-consumable, was securely affixed in the spindle, positioned at a tilt angle of 3° in relation to the AA6082-T6 plate. The chosen tilt angle aims to improve the forging action under the tool shoulder, facilitate efficient material consolidation behind the tool, and minimize the risk of tunnel flaws or voids. Prior research has indicated that both excessive and insufficient tilt angles might result in unstable material flow or surface flaws [1, 14, 23].

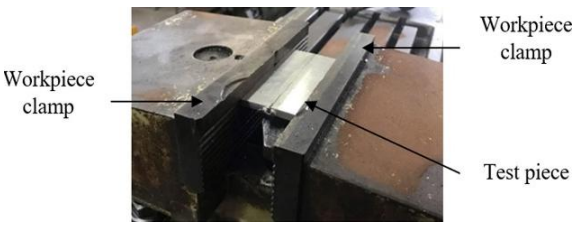


Fig. 3. Clamping and support setup used during the FSW process.

The welding settings were chosen to exemplify low, middle, and high heat-input regimes often documented for friction stir welding of 6xxx-series aluminum alloys [9–11, 24, 25]. Rotational rates of 710, 1,000, and 1,400 rpm were selected because of their significant influence on frictional heat generation, stirring intensity, and plastic flow stability [1, 23, 24].
An intermediate speed of 1,000 rpm is reported to yield a balanced thermal-mechanical state for AA6082-T6, but 710 rpm and 1,400 rpm are associated with limited and elevated heat-input circumstances, respectively [9, 10, 24, 25].
Traverse speeds were established at 14, 28, and 56 mm/min to regulate heat input per unit length and thermal exposure duration. Reduced traverse speed elevates heat input and extends thermal cycles, while increased traverse speed diminishes heat input and hastens cooling, consequently affecting recrystallization behavior and precipitate stability [9, 11, 25, 26].
These parameter combinations facilitated a systematic assessment of the interrelated impacts of heat input and strain rate on material flow, microstructural development, and joint efficacy. This study qualitatively interprets relative heat input by examining the combined effects of rotational speed, which enhances frictional heat generation, and traverse speed, which diminishes heat input per unit length by shortening thermal exposure time. Consequently, elevated rotational speed coupled with increased traverse speed produces high peak temperatures while reducing net heat input per unit length.
All specified settings resulted in fully consolidated joints devoid of macroscopic flaws for the 6 mm thick AA6082-T6 plates. Fig. 4 illustrates a schematic of the experimental setup.

2.5. Friction stir welding procedure

A systematic friction stir welding approach was employed for all welding tests to guarantee uniform heat input and reproducible outcomes. The procedure commenced with the clockwise rotation of the FSW tool, producing frictional heat between the tool shoulder and the aluminum surface. Upon generating sufficient heat, the revolving threaded pin was inserted into the joint line to the requisite depth and maintained for approximately 30 s to guarantee efficient plasticization of the material. The simultaneous application of rotating and downward force during welding resulted in significant plastic deformation, generating vortex-like material movement and efficient mixing inside the stir zone. The tool was thereafter progressed along the weld line at consistent rotational and traverse velocities. This phase converted the malleable substance into the optimal solid-state adhesion. Following welding, the tool remained motionless for 30 s prior to retraction to regulate temperature and avert keyhole development. Fig. 5 illustrates the complete FSW sequence.
Previous research on AA6082-T6 and comparable 6xxx-series aluminum alloys suggests that maximum stir-zone temperatures, under similar rotational and traverse speed parameters, are often documented to range from 450 to 550°C [9–11].
This study utilizes a relative heat-input approach to examine alterations in microstructural evolution and mechanical properties, leveraging established relationships among process variables, thermal exposure, and plastic deformation as documented in existing literature.

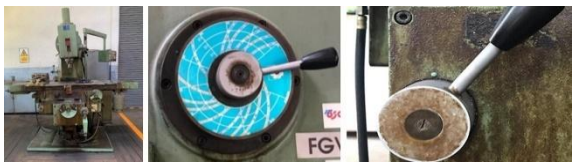

(a) (b) (c)

Fig. 4. Friction stir welding setup: (a) tilting of the vertical milling head, (b) adjustment of tool rotational speed, and (c) adjustment of welding traverse speed.

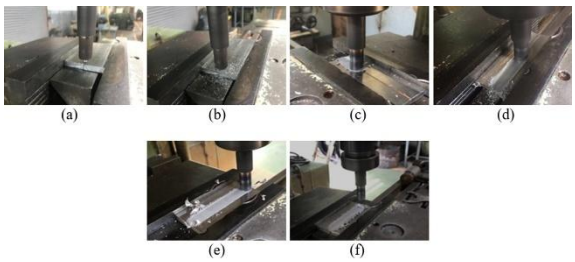

(a) (b) (c) (d) (e) (f)

Fig. 5. Friction stir welding process; (a) tool pin rotating in the clockwise direction, (b) tool pin plunging into the aluminum plate, (c) frictional heat generation, (d) tool traversing at the specified welding speed, (e) joint formation behind the tool, and (f) tool pin retraction after welding.

2.6. Preparation of specimens for macrostructural, microstructural, and mechanical testing

The welded plates were sectioned orthogonally to the welding direction for various mechanical and microstructural evaluations after all friction stir welding investigations were completed. Fig. 6 illustrates the configuration and extraction sites of the test specimens. The cross-section was divided into certain regions: Section A, which included the beginning and end segments of the weld, was removed to reduce temporary temperature impacts. Section B comprised tensile test specimens with a width of 12 mm, whereas Section C included impact test specimens with a width of 8 mm. Section D was designed for metallographic and microhardness studies, measuring 8 mm in width. This systematic segmentation ensured consistent sampling and accurate assessment of mechanical and microstructural properties across different welded areas.

The metallographic samples were mounted in epoxy resin and sequentially ground with silicon-carbide abrasive papers (grit sizes 80–1500), followed by polishing with alumina suspensions of 0.5, 0.3, and 0.1 µm to obtain a mirror-like surface. The macro- and microstructural analyses were carried out using optical microscopy to identify the SZ, TMAZ, HAZ, and BM.

Microhardness assessments were conducted on specimens obtained from region (D), which had previously been utilized for macro- and microstructural evaluations. Before testing, the surfaces were re-polished with a felt cloth and alumina suspensions of particle sizes 0.5, 0.3, and 0.1 µm to attain a smooth, reflective finish conducive to precise indentation.

The assessments were performed using a Vickers microhardness tester (MATSUZAWA Model MMT-X) with a diamond pyramidal indenter. A force of 100 gf (approximately 0.98 N) was applied for 10 s. Indentations were positioned 1 mm apart throughout the transverse cross-section, encompassing the AS, SZ, and RS. Fig. 7 illustrates the indentation layout and testing path. This systematic hardness mapping elucidated the localized strengthening and softening characteristics of several weld areas.

The tensile properties of the friction stir-welded joints were evaluated using samples from region (B) of the welded plates. The samples were manufactured in compliance with ASTM E8M standards, ensuring the weld nugget was accurately centered inside the gauge length.

Experiments were conducted at room temperature (about 25°C) using a universal testing machine (Narin Instrument, Model NRI-TS500-1S) with a crosshead speed of 1 mm/min under quasi-static loading conditions. For each welding condition, three replicate specimens (n = 3) were tested, and the reported values of ultimate tensile strength (UTS), yield strength (YS), and elongation represent the arithmetic mean together with the corresponding standard deviation.

Error bars in the tensile plots indicate ± one standard deviation. Load–elongation data were gathered to determine UTS, YS, and elongation at fracture. The results were employed to assess the influence of rotational and traverse speeds on joint strength and the mechanical characteristics of different weld zones.

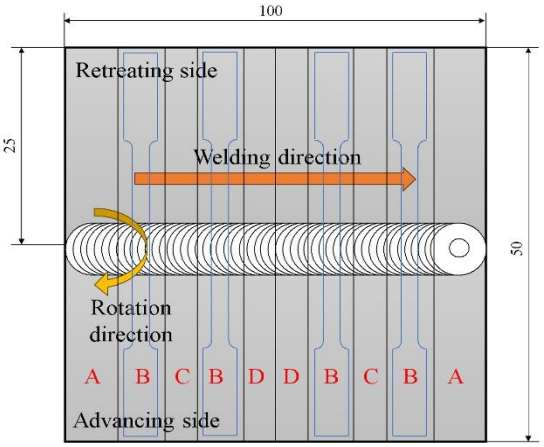


Fig. 6. Schematic diagram showing the cutting layout of the test specimens.

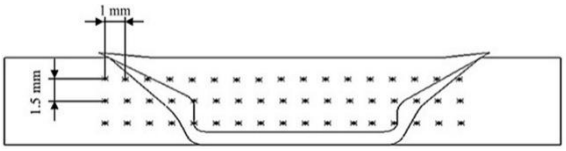


Fig. 7. Schematic illustration showing the indentation positions used for microhardness testing across the welded joint.

The impact toughness of the friction stir-welded joints was assessed using specimens from the region (C) of the welded plates. The surfaces were systematically polished using silicon carbide papers (grit 80–1500) to attain an impeccable finish for accurate energy measurement. Tests were conducted utilizing a WP-410 pendulum impact tester in accordance with the Charpy V-notch methodology, with the notch aligned at the weld centerline.

The machine functioned with a maximum impact energy capability of 300 Nm. For each parameter combination, three Charpy specimens (n = 3) were tested, and absorbed energy values are presented as mean ± standard deviation; the scatter is shown as error bars. Energy absorption values were documented post-fracture to assess the influence of rotational and traverse speeds on weld toughness and the relationship between FSW-induced microstructural refinement and impact performance.

3. Results and discussion

3.1. Surface morphology of the welded joints

The surface morphology of the friction stir-welded AA6082-T6 joints at rotational speeds of 710, 1,000, and 1,400 rpm and traverse speeds of 14, 28, and 56 mm/min is shown in Fig. 8. All parameter combinations yielded welds with uninterrupted seams, devoid of apparent surface-breaking defects, including groove-like discontinuities or severe surface oxidation. Distinct tool shoulder imprints and quantifiable flashes were noted on both the AS and RS.

At higher traverse rates of 56 mm/min, the flash height diminished and the surface exhibited a smoother appearance, whereas a lowered traverse speed of 14 mm/min resulted in thicker flashes, signifying a greater effective heat input per unit length. Elevating the rotational speed from 710 to 1,400 rpm led to enhanced plasticization and lateral material extrusion, in accordance with heightened frictional heating and stirring intensity. Small keyhole-like depressions occasionally manifested just at the weld termination region, resulting from tool withdrawal rather than the creation of internal defects during steady-state welding.

The observations suggest that the combinations of 1,000–1,400 rpm with 28–56 mm/min facilitated stable material flow and balanced heat input, as seen by the symmetric flash patterns and homogenous surface topography. Conversely, the minimal rotational speed of 710 rpm at a low traverse speed resulted in localized irregular flash generation, indicating inadequate softening in certain regions. Current developments corroborate earlier observations that symmetrical flashes and smooth weld surfaces signify balanced thermal–mechanical conditions during FSW [14], while either excessive or inadequate heat input might result in asymmetric flash production or tunnel flaws.

Previous studies [7, 8, 27, 28] have stressed the importance of tool rotation in enhancing heat generation and stabilizing material flow in 6xxx-series aluminum alloys. Additionally, the advantageous impact of integrating moderate rotational speeds with suitable traverse speeds on weld aesthetics and joint efficacy has been documented [29, 30].

The current findings offer more understanding of surface morphology and material flow characteristics in friction stir-welded AA6082-T6 joints. Welds generated at rotational speeds of 1,000–1,400 rpm and traverse rates of 14–28 mm/min displayed extremely symmetrical flash generation and a consistently smooth surface, as illustrated in Fig. 8. This signifies a processing window where plastic flow stabilizes and heat input is sufficiently balanced along the weld line, contrasting with the asymmetric flash production commonly documented for similar alloys and welding conditions in the literature [10, 14].

The uninterrupted surface and completely developed nugget zone evident in these welds indicate efficient three-dimensional material transport and robust metallurgical bonding; this degree of consolidation is comparable to, and in some instances surpasses, that previously documented for friction-stir-welded 6xxx-series aluminum alloys [31, 32].

A minor localized keyhole was detected solely at the weld termination zone, whereas the traversed area was devoid of internal flaws. This characteristic is attributed to tool withdrawal rather than inadequate bonding during welding.

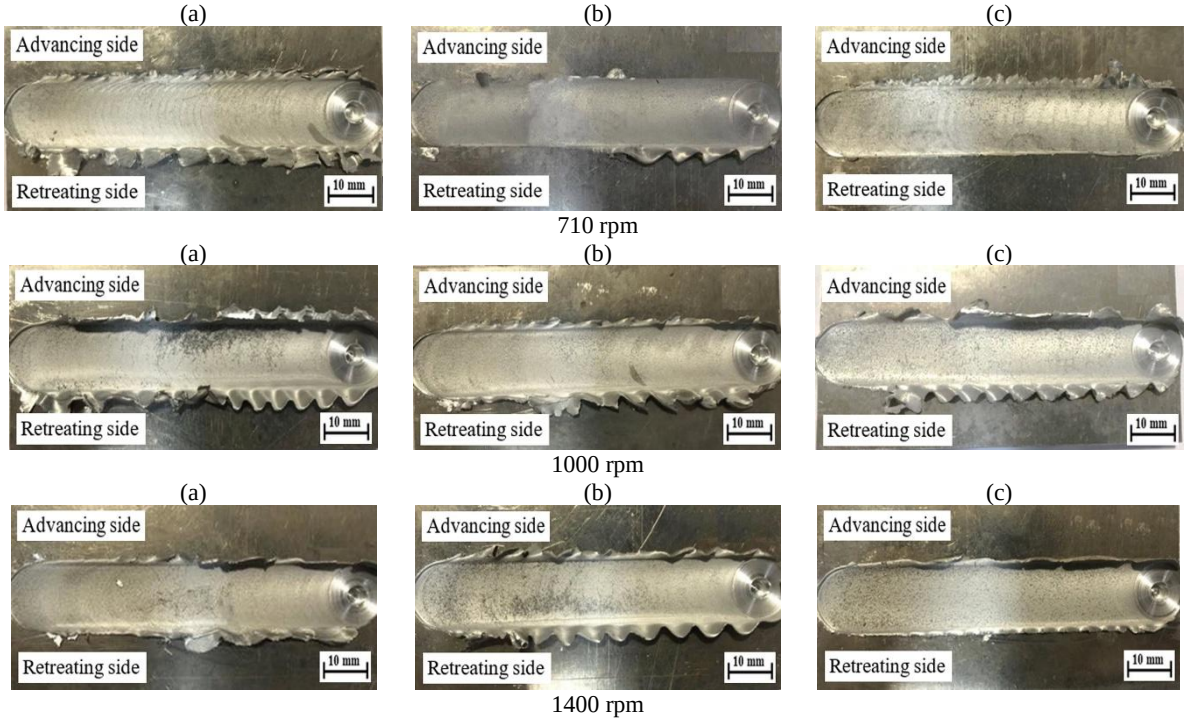


Fig. 8. Top surface morphology of the welds at different rotational speeds with welding traverse speeds of: (a) 14 mm/min, (b) 28 mm/min, and (c) 56 mm/min.

It aligns with exit-keyhole signals documented in thermal modeling and in situ monitoring research [33, 34]. This characteristic is ascribed to tool withdrawal rather than inadequate bonding during welding and aligns with exit-keyhole signals documented in thermal modeling and in situ monitoring research [33, 34]. The strong correlation among smooth surface morphology, symmetric flash, and complete weld penetration observed in this study indicates that surface appearance may function as an effective nondestructive indicator of weld integrity in AA6082-T6 joints, corroborating trends identified in contemporary image-based quality assessment methodologies for FSW [35].

3.2. Macrostructural observation of the welded joints

The friction stir-welded AA6082-T6 joints' macrostructural characteristics are illustrated in Fig. 9 for traverse speeds of 14, 28, and 56 mm/min and rotational speeds of 710, 1,000, and 1,400 rpm. All welds displayed distinctly identifiable SZ, TMAZ, and HAZ regions on both the AS and RS, together with the distinctive onion-ring pattern in the SZ. The continuity of these zones and the lack of voids or tunnel flaws affirm total consolidation across all parameter combinations.

At 710 rpm, the SZ boundary exhibited small irregularities, particularly in the lower section of the nugget, where the breadth grew narrower and less uniform. This morphology aligns with reduced heat input and constrained plasticization; however, the joints exhibited full penetration, signifying that the exerted axial force and tool design were adequate to prevent partial bonding.

Elevating the rotational speed to 1,000 rpm resulted in a more symmetrical nugget with defined onion rings throughout the weld thickness, signifying stable material flow and enhanced thermal–mechanical equilibrium. At 1,400 rpm, the SZ area exhibited a significant increase in size. Despite the absence of internal flaws, the slight deformation observed at the lower AS edge indicates localized overheating and minor flow instability under high-rotation conditions combined with rapid traverse, which produces high peak temperature but reduced heat input per unit length.

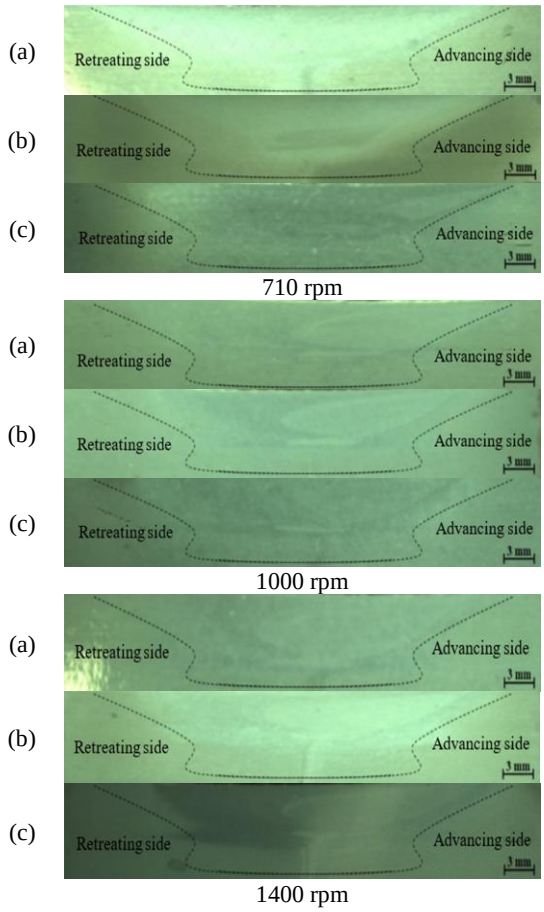


Fig. 9. Macrostructures of friction stir welded joints at different rotational speeds with welding traverse speeds of: (a) 14 mm/min, (b) 28 mm/min, and (c) 56 mm/min.

These findings align with prior studies indicating that inadequate heat input results in poorly mixed areas, whereas excessive heat input may contribute to nugget distortion and grain coarsening [23]. The current findings concur with research identifying rotating speed as the primary determinant of nugget geometry and defect formation in AA6082 and other alloys [36], as well as with reviews associating symmetric flash and uniform macro-geometry with effective internal consolidation [37].

The present analysis not only corroborates prior research but also provides two macrostructural insights. Initially, ideal welds displaying a continuous onion-ring configuration were achieved even at 710 rpm, indicating that adequate dwell time and tool design can compensate for relatively low rotational speeds. The little asymmetry noted at 1,400 rpm indicates the emergence of flow instability under elevated heat-input circumstances. The persistent correlation between surface flash symmetry and nugget uniformity demonstrated herein suggests that surface morphology could serve as a viable indicator of internal weld integrity in AA6082-T6 friction stir welds.

3.3. Microstructural observation of the welded joints

The optical micrographs in Figs. 10–12 illustrate the microstructural characteristics of the friction stir-welded AA6082-T6 joints fabricated at rotational speeds ranging from 710 to 1400 rpm and traverse rates between 14 and 56 mm/min. Under all conditions, the characteristic regions of friction stir welding were identified, specifically the SZ, TMAZ, and HAZ, thereby validating effective solid-state bonding.

At 710 rpm, as illustrated in Fig. 10, the SZ exhibited elongated and partially refined grains oriented in the direction of tool rotation. This shape signifies constrained recrystallization resulting from diminished heat input and strain rate. The TMAZ exhibited plastically distorted grains without complete recrystallization, but the HAZ maintained a morphology similar to the base metal with minimal coarsening.

Augmenting traversal speed during this rotation diminished heat input, resulting in finer yet less uniform grains in the bottom nugget region.

At 1,000 rpm, as illustrated in Fig. 11, the SZ predominantly included fine equiaxed grains. This structure aligns with dynamic recrystallization under moderate thermal input and exhibits the most uniform shape among the assessed conditions. Finer grains were regularly detected on the advancing side compared to the retreating side, indicating more local shear deformation. Transitional substructures in the TMAZ facilitated seamless continuity between the SZ and the base metal. Previous studies [24, 38] showed analogous equiaxed structures at similar velocities in AA6082-T6.

At 1,400 rpm, as illustrated in Fig. 12, the SZ expanded due to increased heat output and intensified plastic flow. Localized coarsening transpired near the upper nugget and on the advancing side, indicating overheating at the maximum rotation level.

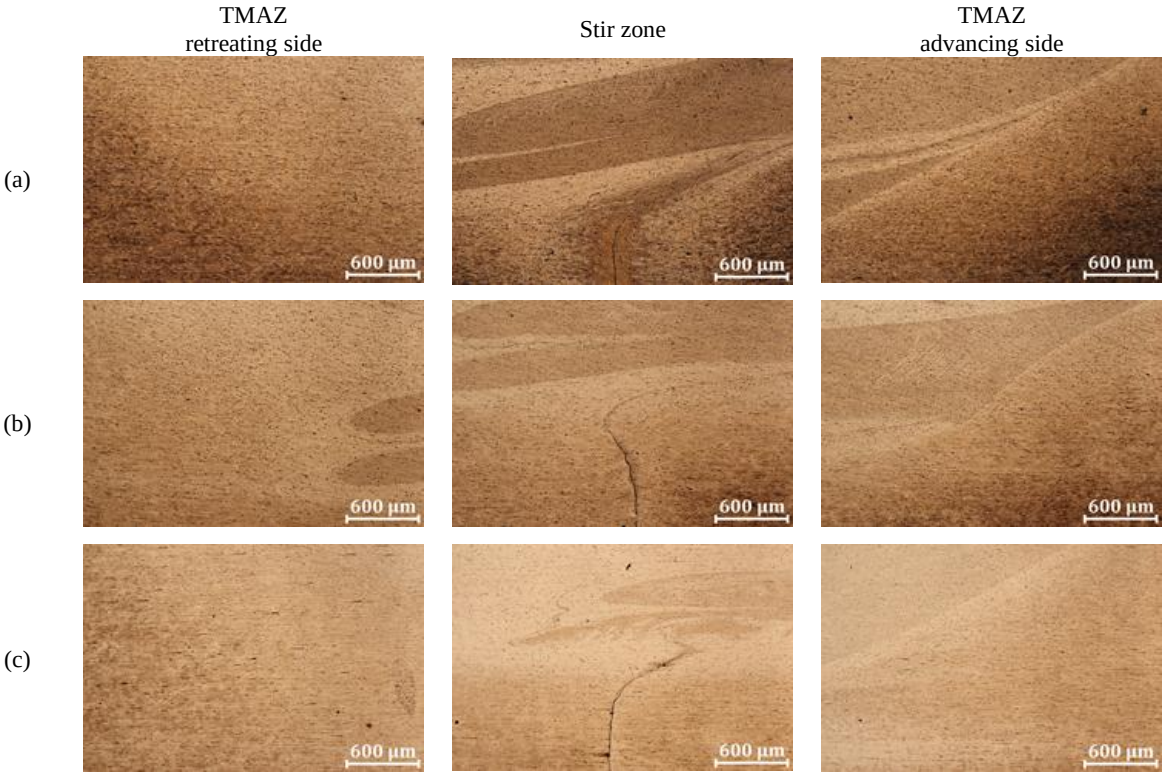


Fig. 10. Microstructures of friction stir-welded joints at different rotational speeds of 710 rpm: (a) 14 mm/min, (b) 28 mm/min, and (c) 56 mm/min.

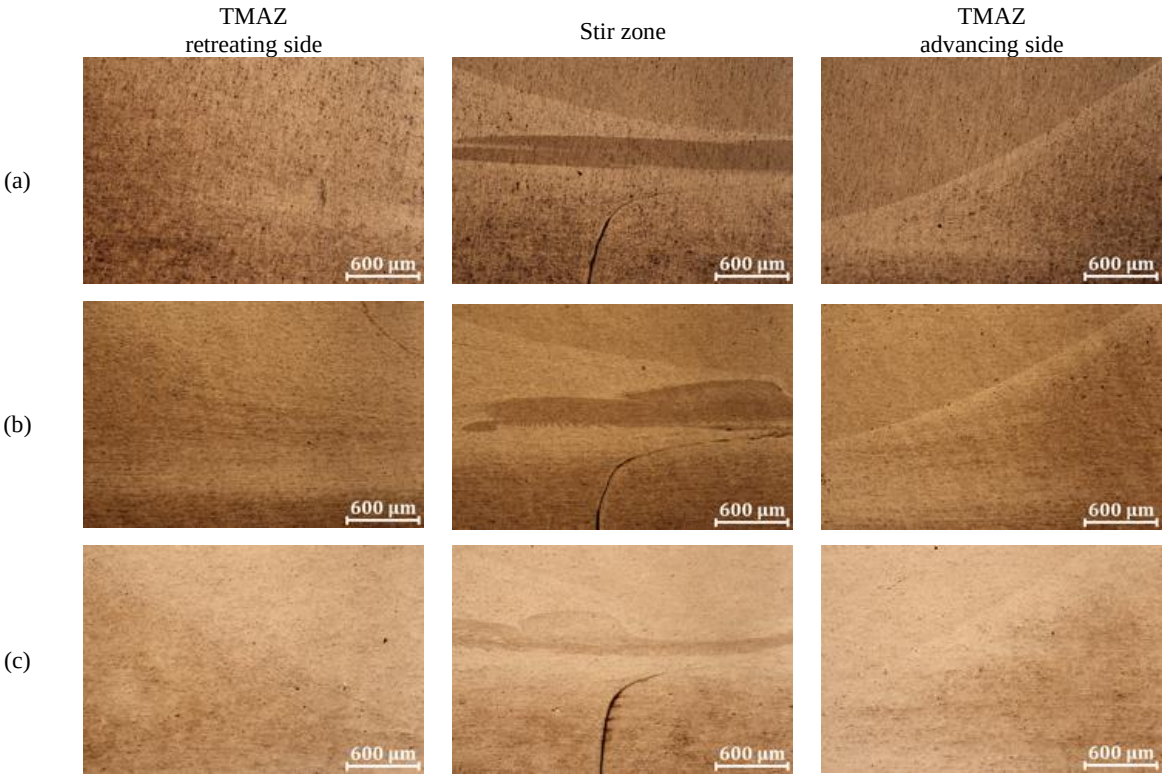


Fig. 11. Microstructures of friction stir-welded joints at different rotational speeds of 1000 rpm: (a) 14 mm/min, (b) 28 mm/min, and (c) 56 mm/min.

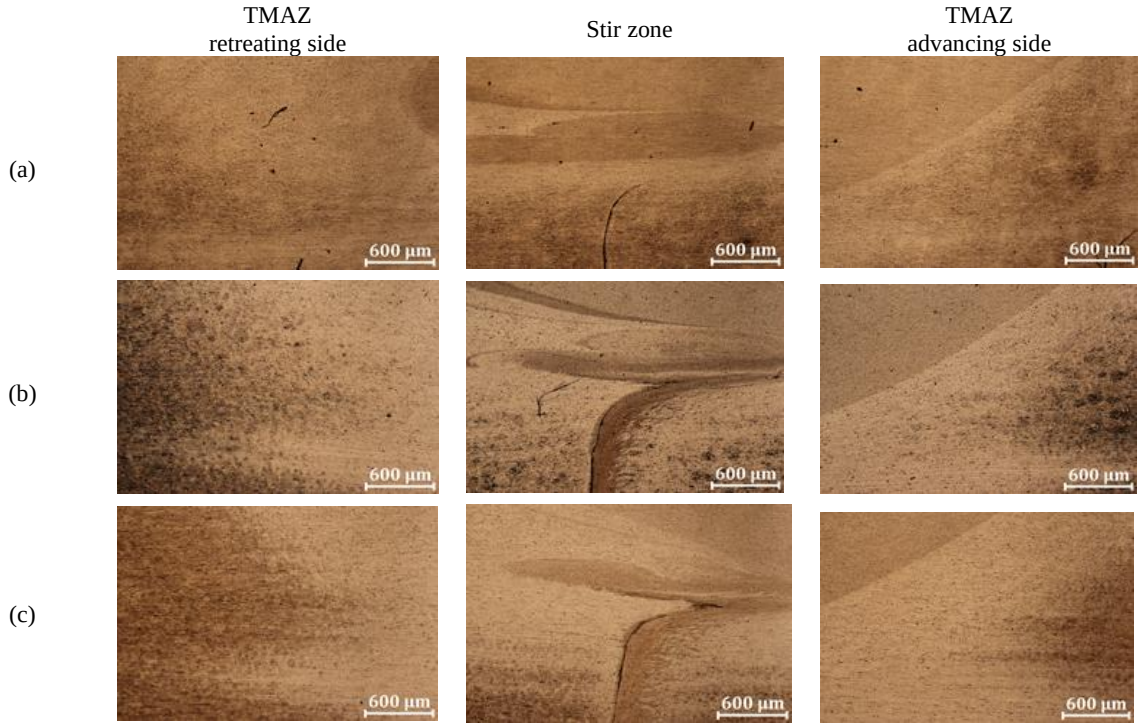


Fig. 12. Microstructures of friction stir-welded joints at different rotational speeds, 1400 rpm of: (a) 14 mm/min, (b) 28 mm/min, and (c) 56 mm/min.

Flow bands exhibited reduced distinctiveness at higher velocities, signifying a decrease in material flow stability at increasing temperatures. These data align with descriptions of microstructural coarsening and flow instability at elevated rotational speeds in 6xxx-series alloys [25]. The results indicate that tool rotation significantly influences the equilibrium between heat input and strain rate, thereby affecting grain shape in the stir zone.

Low rotation (710 rpm) resulted in incomplete recrystallization, intermediate rotation (1,000 rpm) yielded the finest and most uniform grain structure, while high rotation (1,400 rpm) led to localized coarsening. These patterns align with prior reports indicating that moderate tool rotation and intermediate traverse rates enhance the refinement of SZ grains and the regularity of joints in 6xxx alloys [24, 39, 40].

The current findings demonstrate two consistent characteristics across all parameter combinations: (1) the AS displayed finer grains than the RS, and (2) even at the maximum traverse speed of 56 mm/min, the SZ remained entirely consolidated without internal defects. The finer grain size in the AS signifies more plastic deformation and elevated local strain rate due to the combined impacts of tool rotation and traverse motion, which facilitate subgrain fragmentation and encourage dynamic recrystallization in contrast to the RS.

Although an increase in traverse speed diminishes thermal exposure duration, full consolidation of the stir zone at 56 mm/min illustrates that the frictional heat produced by tool rotation and shoulder contact was adequate to soften the material and maintain continuous plastic flow.

Under these circumstances, the synergistic effects of frictional heating and intense plastic deformation resulted in a refined, equiaxed grain structure in the SZ, while the TMAZ displayed elongated and rotated grains, and the HAZ demonstrated thermal overaging without considerable plastic deformation. The microstructural characteristics align with thermally assisted dynamic recrystallization induced by elevated strain and temperature in the SZ, whereas precipitate coarsening and partial dissolution prevail in the HAZ and TMAZ, respectively.

3.4. SEM and EDX characterization of the SZ

The SEM analysis of the stir zone at 1400 rpm and 56 mm/min, illustrated in Fig. 13, demonstrated a dense and defect-free microstructure. Continuous flow striations were evident throughout the nugget, with no voids, oxide coatings, or tunnels detected, signifying thorough material consolidation and stable plastic flow during friction stir welding.

At a magnification of 2500×, fine precipitates were uniformly distributed inside the aluminum matrix. These particles are linked to Mg_2Si, Al_6Mn, and Fe-rich intermetallics commonly seen in AA6082-T6. Their precise dimensions and consistent spatial arrangement suggest fragmentation and redistribution resulting from significant plastic deformation and thermally aided recrystallization in the stir zone [24–27].

The development of this precipitate morphology is intricately associated with the thermal energy produced during welding at 1400 rpm and 56 mm/min. The elevated rotational speed generated adequate frictional heat to partially dissolve coarse primary precipitates, although the relatively high traverse speed restricted the total thermal exposure duration. Upon subsequent cooling, reprecipitation manifested as fine, uniformly distributed particles instead of coarse agglomerates. This integrated thermal–mechanical cycle elucidates the occurrence of ultrafine precipitates and refined equiaxed grains shown in the SEM pictures [31, 32].

The uniform distribution of precipitates facilitates precipitation and dispersion strengthening and aids in stabilizing grain boundaries by impeding boundary motion, and so enhances the hardness and tensile strength seen for this parameter combination.

EDX elemental mapping illustrated in Fig. 14 further confirmed the homogeneous distribution of the key alloying elements throughout the stir zone. The Al map displayed a uniform and entirely consolidated aluminum matrix, verifying the lack of unbonded areas or oxide inclusions. The Mg and Si maps demonstrated a uniform distribution of Mg–Si–rich particles corresponding to Mg_2Si precipitates, whereas Mn-enriched areas were linked to thermally stable Al_6Mn dispersoids. Moreover, finely fragmented Fe-containing intermetallics were observed, suggesting mechanical disintegration and redistribution during agitation.

The consistency of element distribution noted at the welding parameters of 1400 rpm and 56 mm/min demonstrates the synergistic impact of substantial plastic deformation and frictional heat production. The increased rotational speed produced sufficiently high peak temperatures to facilitate partial dissolving of coarse primary Mg_2Si particles, whereas the comparatively high traverse speed constrained the overall heat input per unit length and curtailed extended overaging. During the ensuing cooling phase, reprecipitation manifested as fine, uniformly distributed particles instead of coarse aggregates. This thermomechanical cycle elucidates the transformation from heterogeneous coarse precipitates in the base material to uniformly distributed nanoscale characteristics in the stir zone.

These data align with previous studies, indicating that increased rotational speeds improve stirring, induce fragmentation, and

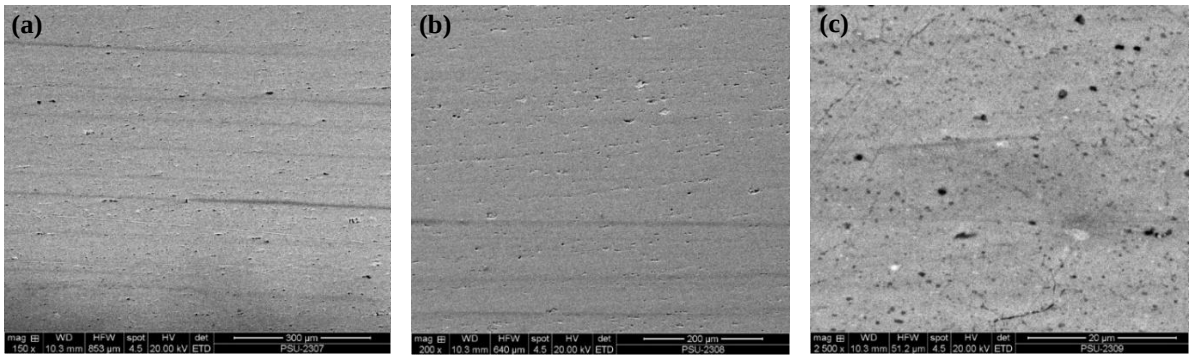


Fig. 13. SEM microstructure of the stir zone of the welded joint at a rotational speed of 1400 rpm and a traverse speed of 56 mm/min: (a) Magnification 150×, (b) Magnification 200×, and (c) Magnification 2500×.

facilitate solute redistribution, subsequently leading to fine reprecipitation during cooling in 6xxx-series aluminum alloys [25, 26, 41]. The current findings demonstrate that precipitate refinement occurs simultaneously with grain refinement, leading to a combined effect of precipitation and grain-boundary strengthening.
The integrated SEM and EDX investigations demonstrate that high-rotation FSW conditions yield a fully consolidated stir zone, distinguished by refined equiaxed grains and uniformly dispersed strengthening precipitates. This uniform microstructure offers a mechanistic rationale for the enhanced hardness and tensile strength achieved under identical parameters.

3.5. Tensile properties

The tensile characteristics of the friction stir-welded AA6082-T6 joints are encapsulated in Table 2 and Fig. 15, whilst the trends associated with process factors are illustrated in Fig. 16. The ultimate tensile strength (UTS) varied between 83.88 and 111.77 MPa, the yield strength between 75.98 and 102.93 MPa, and the elongation between 5.64% and 10.44%, demonstrating a significant correlation with tool rotating speed and traverse speed. The maximum UTS of 111.77 MPa was achieved at 1400 rpm and 56 mm/min, while the minimum UTS of 83.88 MPa was recorded at 1000 rpm and 14 mm/min.
Fig. 16 illustrates that tensile strength often escalated with the augmentation of rotational speed from 710 to 1400 rpm, a phenomenon attributable to enhanced frictional heating and plastic flow that facilitate grain refining in the SZ. For each rotational speed, augmenting the traverse speed from 14 to 56 mm/min improved tensile strength, attributable to diminished heat input per unit length and the mitigation of precipitate coarsening [39].
The ultimate tensile strength of the welded joints, 83.88–111.77 MPa, is markedly inferior to that of the AA6082-T6 base material (≈ 290–320 MPa), a decline that aligns with previously documented behavior of friction stir-welded 6xxx-series alloys in the T6 condition. The decrease in strength is principally attributable to HAZ softness caused by the dissolution and coarsening of Mg_2Si precipitates during welding, with fractures predominantly occurring in the HAZ/TMAZ rather than the stir zone.

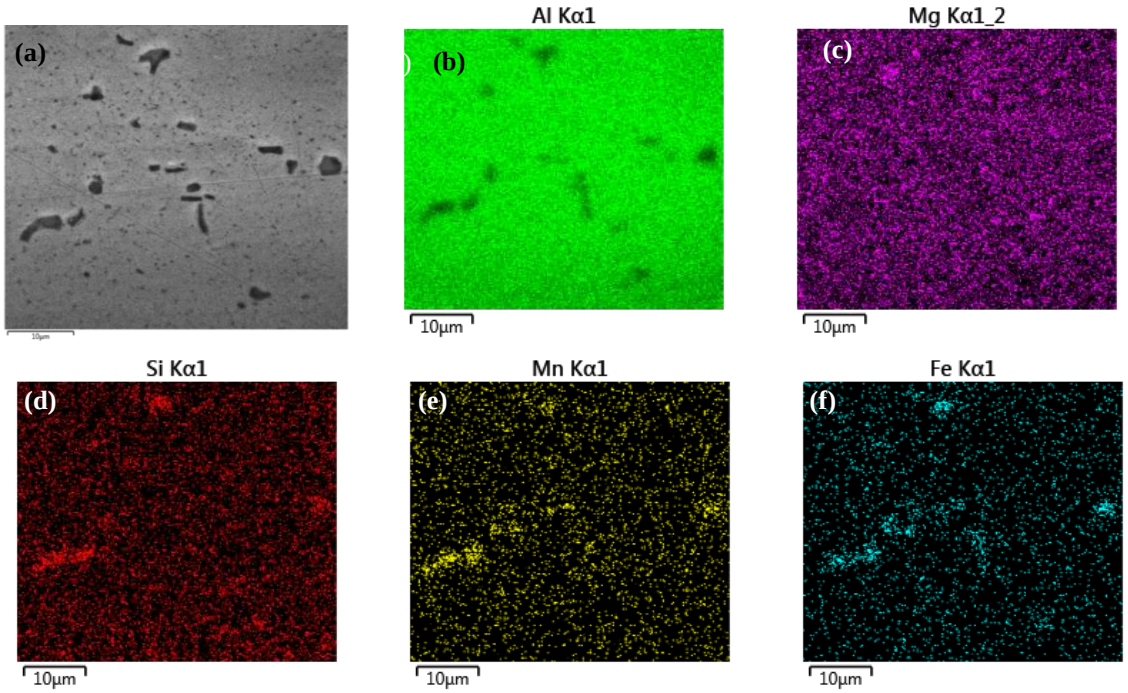


Fig. 14. EDX elemental mapping of the stir zone of the welded joint at a rotational speed of 1400 rpm and a traverse speed of 56 mm/min: (a) zone of elemental mapping, (b) elemental Al, (c) elemental Mg, (d) elemental Si, (e) elemental Mn, and (f) elemental Fe.

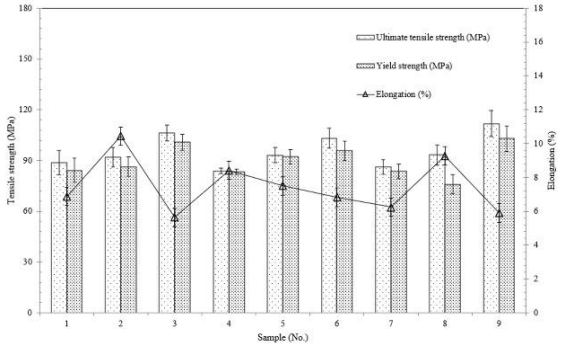


Fig. 15. The tensile strength, yield strength and elongation of the welded joints under different welding conditions.

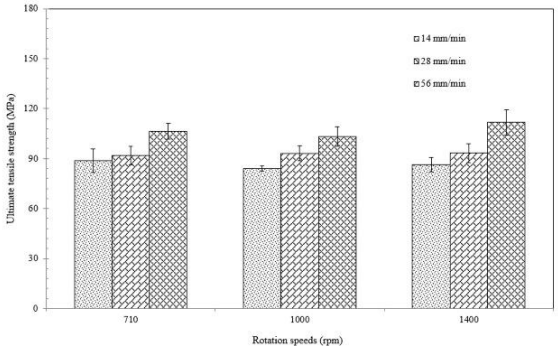


Fig. 16. Variation of tensile strength with different welding traverse speeds.

Table 2. Tensile properties of the friction stir welded AA6082-T6 joints.

Sample (No.)	Rotation speed (rpm)	Welding speed (mm/min)	Tensile stress (MPa)	Yield stress (MPa)	Elongation (%)	Joint efficiency (%)
1	710	14	88.70	84.19	6.88	30.59
2	710	28	91.93	86.38	10.44	31.70
3	710	56	106.35	100.75	5.64	36.67
4	1000	14	83.88	83.24	8.42	28.92
5	1000	28	93.20	92.20	7.51	32.14
6	1000	56	103.18	95.73	6.83	35.58
7	1400	14	86.31	83.56	6.24	29.76
8	1400	28	93.23	75.98	9.28	32.15
9	1400	56	111.77	102.93	5.90	38.54

At 710 rpm, tensile strength significantly increased with higher traverse speed, indicating that the augmented plastic deformation and improved stirring offset the limited heat input per unit length. Increased traversing speed mitigated excessive heat buildup, maintained finer precipitates, and averted over-softening in the TMAZ, consequently enhancing load-bearing capability. At 1000 rpm, the tensile strength stabilized at around 103 MPa, signifying a processing regime where the thermal and mechanical fields were well balanced to provide significant grain refinement in the stir zone while preventing substantial precipitate coarsening.

The maximum tensile strength achieved at 1400 rpm and 56 mm/min aligns with the defect-free macrostructure and uniform precipitate dispersion demonstrated by the SEM and EDX tests. Under these conditions, vigorous agitation and sufficient peak temperature facilitated considerable microstructural refinement in the stir zone, while the relatively brief thermal exposure linked to the high traverse speed restricted precipitate over-aging. This combination enabled effective stress transfer across the nugget zone, leading to enhanced joint strength.

The changes in tensile behavior can be ascribed to the combined impacts of grain refinement strengthening and precipitate evolution. Under moderate to high heat input settings, 1000–1400 rpm and 28–56 mm/min, the studied microstructures exhibited significant recrystallization, resulting in thin equiaxed grains that enhance strength via the Hall–Petch relationship.

The concurrent fragmentation, partial dissolving, and subsequent redistribution of Mg_2Si and Al_6Mn dispersoids enhanced precipitation strengthening in the stir zone. Conversely, at a low traverse speed of 14 mm/min, the extended temperature exposure facilitated precipitate coarsening and over-aging in the TMAZ and HAZ, leading to localized softness and diminished joint performance. This tendency aligns with earlier observations in AA6082-T6 friction stir-welded joints, where the softest region dictates tensile failure instead of the fully refined stir zone [24, 25].

The link between strength and ductility aligns with the anticipated trend for heat-treatable 6xxx alloys. The joint fabricated at 1400 rpm and 56 mm/min demonstrated the highest ultimate tensile strength with moderate elongation of about 5.9%, indicating enhanced dislocation density and fine precipitate distribution that impede plastic flow.

Fig. 17 illustrates the fracture characteristics of tensile specimens obtained from friction stir-welded AA6082-T6 joints, reflecting the maximum tensile strength attained at each rotational speed: (a) 710 rpm and 56 mm/min, (b) 1,000 rpm and 56 mm/min, and (c) 1,400 rpm and 56 mm/min. Fractures consistently occurred outside the immediate weld centerline, primarily within the TMAZ or the neighboring HAZ, thereby demonstrating that the SZ exhibited greater strength compared to the surrounding areas.

The joint welded at 710 rpm and 56 mm/min, Fig. 17(a), displays significant necking and an angled fracture plane, signifying a ductile failure mode characterized by plastic deformation. The reduced rotating speed, coupled with elevated traverse speed, led to little heat input, hence preventing excessive grain development while maintaining adequate flexibility in the TMAZ. Comparable fracture behavior has been shown for low-to-moderate heat input friction stir welded joints of AA6082-T6, wherein ductile fracture correlates with partially recrystallized grains and preserved precipitate strengthening [24].

At 1,000 rpm and 56 mm/min, Fig. 17(b), the tensile specimen exhibits significant necking and a more homogeneous fracture surface, indicating an ideal equilibrium between strength and ductility.

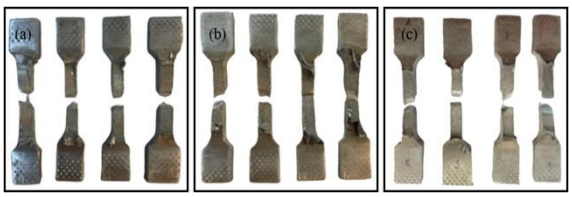


Fig. 17. Tensile fracture appearances of friction stir welded AA6082-T6 joints corresponding to the highest tensile strength at each rotational speed: (a) 710 rpm and 56 mm/min, (b) 1000 rpm and 56 mm/min, and (c) 1400 rpm and 56 mm/min.

This scenario generated sufficient frictional heat and stirring intensity to facilitate microstructural features that are consistent with and suggestive of DRX mechanisms refinement in the stir zone and provide a somewhat uniform microstructure across the joint. The enhanced tensile performance and ductile fracture morphology align with prior research indicating that intermediate rotational speeds improve plastic flow stability and mitigate premature failure in the TMAZ [10, 25].

Conversely, the specimen welded at 1,400 rpm and 56 mm/min Fig. 17(c), demonstrates diminished necking and a relatively flatter fracture surface, signifying a shift towards a mixed ductile–brittle fracture mode. Despite this condition producing the greatest tensile strength, the augmented rotating speed resulted in enhanced strain rates and increased dislocation density, hence diminishing local ductility in the TMAZ. This behavior is ascribed to excessive grain refinement and localized over-hardening, which impede plastic deformation during tensile loading [41, 42].

3.6. Hardness distribution

The microhardness profiles measured across the weld cross-sections are shown in Fig. 18(a–c) for different combinations of tool rotational speeds 710–1400 rpm and traverse speeds 14–56 mm/min. All joints displayed the characteristic "W-shaped" hardness distribution, with the minimum hardness located in the HAZ and increased hardness towards the SZ. This phenomenon is typical of precipitation-hardened 6xxx-series alloys and is ascribed to the dissolving of Mg_2Si in the heat-affected zone and the subsequent reprecipitation and grain refinement within the stir zone [26].

At 710 rpm, as illustrated in Fig. 18(a), the peak hardness attained was 70.03 HV at a feed rate of 56 mm/min, while the lowest value of 51.07 HV was recorded at 14 mm/min. The significant variance suggests that, at low rotational speeds, hardness is markedly responsive to traverse speed. At 14 mm/min, inadequate stirring and localized over-aging led to HAZ softening, while at 56 mm/min, diminished heat input per unit length restricted precipitate coarsening and encouraged finer grains, yielding increased hardness.

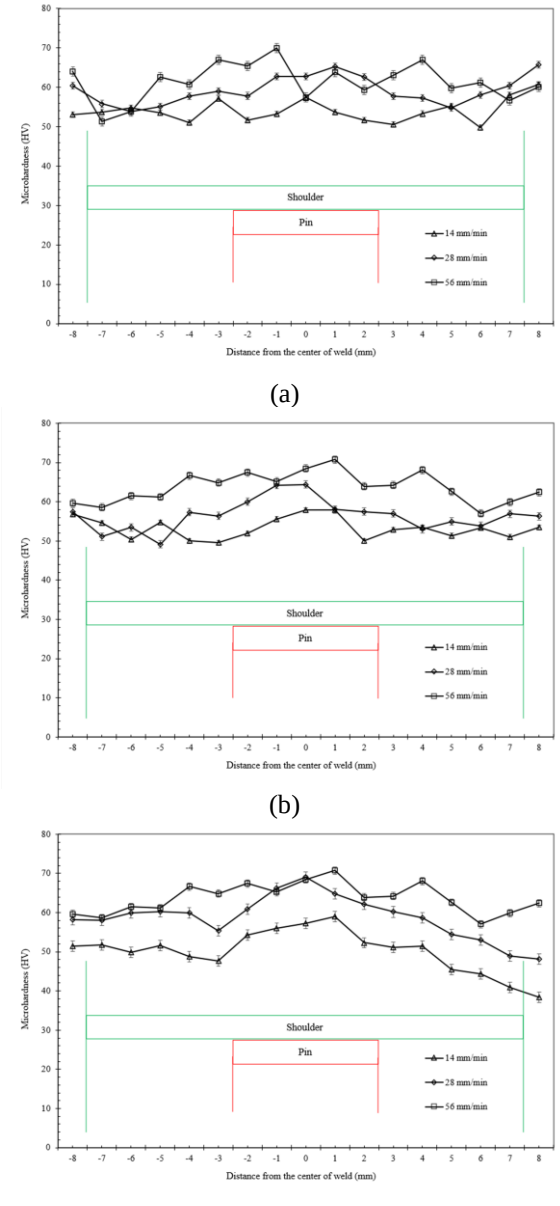


Fig. 18. Microhardness profiles across the weld cross-sections at different rotational speeds: (a) 710 rpm, (b) 1000 rpm, and (c) 1400 rpm.

At 1000 rpm, as illustrated in Fig. 18(b), the hardness profiles exhibited increased uniformity. The maximum value of 70.73 HV was recorded at 56 mm/min, whereas the minimum value of 49.17 HV was seen at 28 mm/min. This parameter range resulted in a more equilibrated thermal-mechanical state, facilitating microstructural features consistent with DRX mechanisms refinement and uniform redistribution of Mg_2Si in the SZ, while preventing significant over-aging in the HAZ.

At 1400 rpm, as illustrated in Fig. 18(c), hardness reached a maximum of 73.77 HV at 56 mm/min, while the minimum value of 45.40 HV was recorded at 14 mm/min. The amalgamation of rapid rotation and swift traverse velocity generated increased strain rates with minimal temperature exposure, facilitating grain refinement and fine precipitate reprecipitation. In contrast, 1400 rpm and 14 mm/min produced excessive thermal input, resulting in the coarsening of strengthening precipitates and significant softening of the HAZ.

In general, hardness escalated with both rotational and traverse speeds, with the highest values at 1400 rpm and 56 mm/min. This relationship follows the Hall–Petch phenomenon, in which smaller grains and uniformly distributed nanoscale precipitates impede dislocation movement and increase hardness. The present findings correspond with prior studies on FSW of AA6082-T6 and analogous alloys, which recorded W-shaped hardness profiles and HAZ softening linked to precipitate dissolution and over-aging. [24–26, 41].

The relationship between hardness and tensile strength is evident: the maximum hardness (~74 HV) at 1400 rpm and 56 mm/min aligns with the highest ultimate tensile strength of 111.77 MPa, suggesting that joint strength is predominantly affected by grain refinement and precipitate redistribution in the stir zone, whereas the softened heat-affected zone is the weakest region.

3.7. Impact Toughness

The absorbed impact energies of the friction stir-welded AA6082-T6 joints are presented in Fig. 19 for different combinations of tool rotational speeds and traverse speeds. The impact toughness values ranged from 9.50 to 13.00 Nm, dependent on the welding parameters. The maximum absorbed energy of 13.00 Nm was observed at 1000 rpm and 14 mm/min, while the minimum value of 9.50 Nm occurred at 710 rpm and 56 mm/min.

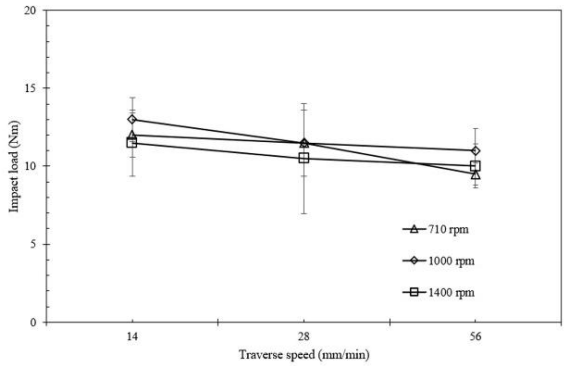


Fig. 19. Impact toughness of the welded joints.

At a constant rotating speed, the absorbed energy generally dropped as the traverse speed increased. This suggests that plastic flow and metallurgical bonding between the advancing and retreating sides of the weld were restricted by lower heat input per unit length and shorter thermal exposure. At 710 rpm, inadequate frictional heating caused partial plasticization and limited dynamic recrystallization, leading to diminished impact toughness. Elevating the rotational speed to 1000 rpm achieved a more advantageous equilibrium between heat input and deformation rate, facilitating equiaxed recrystallized grains in the stir zone and resulting in optimal impact toughness.

At the maximum rotating speed of 1400 rpm, the impact toughness diminished, notwithstanding the elevated hardness and tensile strength achieved under the same conditions. This decrease is ascribed to elevated strain rates and swift cooling, resulting in extremely small grains with high dislocation density and residual stresses, therefore inhibiting plastic deformation under impact loading and facilitating a mixed ductile–brittle fracture mode.

These trends align with previous research on AA6082-T6 friction stir welding, indicating that moderate heat input facilitates complete dynamic recrystallization and optimizes energy absorption, while excessively low or high heat input results in either inadequate bonding or embrittlement [24, 25, 41, 42]. The current findings demonstrate that the impact toughness in AA6082-T6 FSW joints is influenced by the interplay of heat input, recrystallization extent, precipitate state, and residual stresses, with optimal conditions achieved at 1000 rpm and 14 mm/min in this investigation.

Fig. 20(a–c) illustrates the fracture characteristics of friction stir-welded AA6082-T6 joints following Charpy impact testing, corresponding to the welding conditions that exhibited the largest impact energy at each rotational speed, all performed at a constant traverse speed of 14 mm/min.

The joint welded at 710 rpm and 14 mm/min, as illustrated in Fig. 20(a), has cracked specimens that demonstrate significant bending before ultimate separation, signifying a somewhat ductile fracture behavior. The fracture surface exhibits considerable irregularity, characterized by localized tearing in the weld area. This behavior indicates restricted plastic flow and inadequate homogeneity in the stir zone, resulting from insufficient heat input at the reduced rotational speed. Thus, despite some plastic deformation before fracture, the overall energy absorption capacity remained low [24].

Conversely, the joint welded at 1,000 rpm and 14 mm/min, illustrated in Fig. 20(b), has the most notable plastic deformation before fracture, marked by considerable specimen bending and a progressive ripping pattern. This condition reflects the highest recorded impact toughness, signifying a prevailing ductile fracture process. The enhanced impact performance is due to a balanced thermal-mechanical state that facilitates uniform dynamic recrystallization, refined equiaxed grains in the stir zone, and regulated redistribution of Mg_2Si precipitates.

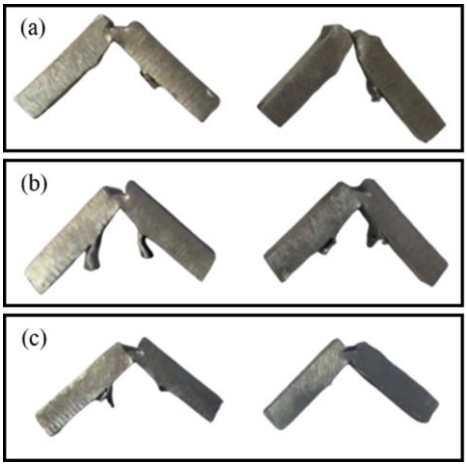


Fig. 20. Impact fracture appearances of friction stir-welded AA6082-T6 joints tested under Charpy impact loading at a traverse speed of 14 mm/min: (a) 710 rpm, (b) 1000 rpm, and (c) 1400 rpm.

These microstructural characteristics promote crack blunting and retard crack development under dynamic stress conditions [27].

For the joint fabricated at 1,400 rpm and 14 mm/min illustrated in Fig. 20(c), fracture transpired with relatively less plastic deformation and a more sudden separation. Despite the weld demonstrating adequate consolidation, the fracture morphology suggests a shift towards a more brittle behavior. The elevated rotational speed enhances strain rate and dislocation density, resulting in a refined yet comparatively harder microstructure that limits plastic deformation under impact loading [42]. The absorbed impact energy diminishes relative to the optimal condition at 1,000 rpm.

The fracture analysis indicates that a moderate rotating speed of 1,000 rpm, together with a low traverse speed, achieves the optimal equilibrium among dynamic recrystallization, precipitate stability, and residual stress relaxation, hence enhancing impact toughness. These findings align with prior research on FSW of Al–Mg–Si alloys, indicating that excessive grain refinement and elevated dislocation density may diminish impact resistance, notwithstanding enhancements in strength and hardness.

3.8. Integrated discussion: correlation among process parameters, microstructure, and mechanical properties

The results of the present study show a clear correlation between friction stir welding parameters, the resulting microstructure, and the mechanical properties of AA6082-T6 joints. Variations in tool rotational speed and traverse speed determined the thermal–mechanical conditions, which in turn governed dynamic recrystallization, precipitate evolution, and residual stress distribution across the weld.

3.8.1. Process parameters and thermal–mechanical balance

The thorough examination of macrostructure shown in Fig. 9, microstructure shown in Figs. 10–12, hardness shown in Fig. 18, and tensile/impact outcomes shown in Fig. 15 and Fig. 19, respectively, confirms that heat input and strain rate are simultaneously affected by rotational and traversal speeds. At a rotational speed of 710 rpm, inadequate heat input indicates the presence of dynamic recrystallization mechanisms and uneven nugget boundaries. At 1000 rpm, a balance of thermal energy and deformation results in a stable nugget and equiaxed grains. At 1400 rpm and 56 mm/min, significant strain and short thermal exposure yield ultrafine grains, whereas at 1400 rpm and 14 mm/min, excessive heat results in coarsening inside the HAZ and TMAZ [43].

3.8.2. Microstructural evolution

Microstructural evidence shown in Figs. 10–12 demonstrates parameter-dependent grain refinement, characterized by elongated and partially recrystallized grains at a rotational speed of 710 rpm, fine equiaxed grains (~5–7 μm) exhibiting complete dynamic recrystallization at 1000 rpm, and ultrafine grains with partial coarsening at the upper nugget at 1400 rpm.

EDX mapping, as shown in Fig. 14, confirmed the displacement of Mg_2Si and Al_6Mn precipitates in the stir zone at increased rotational speeds. Grain refinement enhanced hardness, whereas localized coarsening or inadequate dynamic recrystallization reduced it.

3.8.3. Mechanical correlation

The mechanical behavior aligned with microstructural trends, exhibiting a maximum tensile strength of 111.77 MPa at 1400 rpm and 56 mm/min, correlated with ultrafine grains and uniform precipitate distribution; a maximum hardness of 73.77 HV under the same conditions; a maximum impact toughness of 13.00 Nm at 1000 rpm and 14 mm/min, linked to balanced grain refinement and reduced residual stress; and a minimum toughness of 9.50 Nm at 710 rpm and 56 mm/min, associated with insufficient plasticization and inadequate interfacial adhesion. Consequently, strength augmented with refining; however, toughness diminished due to excessive strain rate or residual stress.

3.8.4. Mechanistic interpretation

The aggregated findings suggest the subsequent mechanisms consists of grain refinement strengthening via the Hall–Petch effect in the stir zone, precipitation strengthening through fragmentation and reprecipitation of Mg_2Si/ Al_6Mn, toughness reduction due to high dislocation density and residual stress at elevated RPM, and softening from precipitate coarsening in the heat-affected zone at low traverse speeds. Dynamic recrystallization predominantly influenced the mechanical characteristics.

The increase in hardness and tensile strength at 1400 rpm and 56 mm/min is primarily attributed to Hall–Petch grain refinement and uniform redistribution of Mg_2Si precipitates in the stir zone, whereas the reduced impact toughness is associated with high dislocation density and residual stresses that limit crack blunting.

3.8.5. Optimal processing window

Two performance regimes arise from the combined data: strength-dominated at 1400 rpm and 56 mm/min, exhibiting maximum hardness and ultimate tensile strength, and toughness-dominated at 1000 rpm and 14–28 mm/min, demonstrating the highest absorbed impact energy. Consequently, parameter selection is contingent upon service requirements rather than a singular "optimal" situation.

4. Conclusions

This study systematically assessed the impact of rotational and traverse speeds on the microstructural development and mechanical characteristics of friction stir-welded AA6082-T6 aluminum alloy joints. All welding settings yielded sound joints devoid of tunnel flaws or voids, demonstrating that the chosen tool material, geometry, and process configuration facilitated stable material flow and thorough consolidation. The emergence of symmetrical flashes and uniform nugget morphologies indicated precisely regulated thermal-mechanical conditions during welding.

The stir zone displayed polished equiaxed grains, with variations in size and homogeneity dependent on process parameters. Elevating rotational speed augmented plastic deformation and facilitated grain refinement, while high heat input at 1400 rpm resulted in localized grain coarsening in certain areas. Finer granules were qualitatively seen on the advancing side in contrast to the retreating side, indicating asymmetric deformation and strain partitioning during welding. SEM–EDX investigations revealed a rather uniform redistribution of Mg_2Si and Al_6Mn precipitates at elevated rotational and traverse speeds, aligning with the fragmentation and re-dispersion of strengthening phases during vigorous stirring.

The mechanical response of the joints was determined by the equilibrium between thermal input and strain rate. The maximum hardness (≈73.8 HV) and tensile strength (≈111.8 MPa) were achieved at 1400 rpm and 56 mm/min, with refined grains and uniformly dispersed precipitates facilitating improved strengthening. The peak impact toughness (≈13.0 Nm) was attained at 1000 rpm and 14 mm/min, where mild temperature exposure facilitated ductile deformation and efficient energy absorption. The joint efficiency for AA6082-T6 base material was found to be about 35–39%, which is in line with the fact that the failure happened mostly in the softened heat-affected zone, which is typical of friction stir-welded heat-treatable 6xxx-series alloys.

The results indicate that optimum combinations of rotational and traversal speeds can be adjusted to achieve either strength-dominant or toughness-dominant performance. A strength-focused regime was discovered at approximately 1400 rpm and 56 mm/min, whereas a toughness-focused regime was noted around 1000 rpm and 14–28 mm/min. These findings emphasize that regulating thermal–mechanical conditions and the resultant grain refinement and precipitate development are crucial for attaining an optimal strength–ductility balance in friction stir-welded AA6082-T6 joints.

Acknowledgment

This research was financially supported by the revenue budget, Rajamangala University of Technology Srivijaya.

References

[1] R. S. Mishra and Z. Y. Ma, "Friction stir welding and processing", *Mater. Sci. Eng., R.*, Vol. 50, No. 1-2, pp. 1-78, (2005).

[2] No. US5460317A. US. *Friction stir welding*, W. M. Thomas, E. D. Nicholas, J. C. Needham, M. G. Murch, P. Temple-Smith and C. J. Dawes, (1995).

[3] V. Rajkumar, M. Venkateshkannan and A. Natarajan, "Friction stir welding of aluminum alloys", *Friction Stir Welding of Aluminium Alloys.*, Eds. S. Sivasankaran, IntechOpen, London, pp. 81-97, (2017).

[4] P. Cavaliere, "Friction stir welding of Al alloys: analysis of processing parameters affecting mechanical behavior", *Procedia. CIRP.*, Vol. 11, pp. 139-144, (2013).

[5] B. M. Zhao, M. Hu, J. Zhu, Z. Y. Han, H. Q. Sun and Y. L. Ji, "Study on two-step aging technology of 6082 aluminum bumper", *Key Eng. Mater.*, Vol. 764, pp. 245-251, (2018).

[6] P. Cavaliere, E. Cerri and A. Squillace "Mechanical response of 2024-7075 aluminium alloys joined by friction stir welding", *J. Mater. Sci.*, Vol. 40, No. 14, pp. 3669-3676, (2005).

[7] Y. Tang, W. Li, Y. Zou, W. Wang, Y. Xu, A. Vairis and G. Çam, "Effects of tool rotation direction on microstructure and mechanical properties of 6061 aluminum alloy joints by the synergistically double-sided friction stir welding", *J. Manuf. Process.*, Vol. 126, pp. 109-123, (2024).

[8] L. Zhang and X. Wang, "Microstructure evolution and properties of friction stir welding joint for 6082-T6 aluminum alloy", *Mater. Res.*, Vol. 21, No. 6, e20180285, (2018).

[9] M. Arab and M. Zemri, "Optimization of process parameters on friction stir welding of AA 6082-T6 butt joints using taguchi method", *Mech. Mech. Eng.*, Vol. 22, No. 4, pp. 1371–1380, (2018).

[10] A. Naumov, I. Morozova, E. Rylkov, A. Obrosov, F. Isupov, V. Michailov and A. Rudskoy, "Metallurgical and mechanical characterization of high-speed friction stir welded AA 6082-T6 aluminum alloy", *Mater.*, Vol. 12, No. 24, 4211, (2019).

[11] J. Adamowski and M. Szkodo, "Friction stir welds (FSW) of aluminium alloy AW6082-T6", *J. Achiev. Mater. Manuf. Eng.*, Vol. 20, No. 1-2, pp. 403-406, (2007).

[12] S. Verma, Meenu and J.P. Misra, "Study on temperature distribution during friction stir welding of 6082 aluminum alloy", *Mater. Today Proc.*, Vol. 4, No. 2, pp. 1350-1356, (2017).

[13] X. H. Zeng, Peng Xue, D. Wang, D.R. Ni, B. L. Xiao, K. S. Wang and Z.Y. Ma, "Material flow and void defect formation in friction stir welding of aluminium alloys", *Sci. Technol. Weld. Joi.*, Vol. 23, No. 8, pp. 1-10, (2018).

[14] K. Kumar and S. V. Kailas, "The role of friction stir welding tool on material flow and weld formation", *Mat. Sci. Eng. A.*, Vol. 485, No. 1-2, pp. 367-374, (2008).

[15] V. Msomi, S. N. Mabuwa and A. Merdji, "Correlation between heat input and mechanical properties of submerged friction stir processed TIG- welded AA8011/AA6082 dissimilar joint: sampling aspect", *Pak. J. Engg. Appl. Sci.*, Vol. 30, pp. 23-33, (2022).

[16] J. Kumar, G. Kumar, H. Mehdi and M. Kumar, "Optimization of FSW parameters on mechanical properties of different aluminum alloys of AA6082 and AA7050 by response surface methodology", *Int. J. Interact. Des. Manuf.*, Vol. 18, pp. 1359-1371, (2024).

[17] S. Mabuwa, V. Msomi, H. Mehdi and K.K. Saxena, "Effect of material positioning on Si-rich TIG welded joints of AA6082 and AA8011 by friction stir processing", *J. Adhes. Sci. Technol.*, Vol. 37, No. 17, pp. 2484-2502, (2023).

[18] H. Mehdi and R.S. Mishra, "An experimental analysis and optimization of process parameters of AA6061 and AA7075 welded joint by TIG+FSP welding using RSM", *Adv. Mater.*

Process. Technol., Vol. 8, No. 1, pp. 598-620, (2022).

[19] S. Jain, R.S. Mishra and H. Mehdi, "Influence of SiC microparticles and multi-pass FSW on weld quality of the AA6082 and AA5083 dissimilar joints", *Silicon.*, Vol. 15, pp. 6185-6197, (2023).

[20] M.S.B. Reyaz, A.N. Sinha, H. Mehdi, and Q. Murtaza, "Effect of pulsed TIG welding parameters on the microstructural evolution and mechanical properties of dissimilar AA6061-T6 and AA7075-T6 weldments", *Arab. J. Sci. Eng.*, Vol. 49, pp. 10891-10911, (2024).

[21] H. Mehdi, S. Jain, V. Msomi, and C. Malla, "Effect of intermetallic compounds on mechanical and microstructural properties of dissimilar alloys Al-7Si/AZ91D", *J. Mater. Eng. Perform.*, Vol. 33, pp. 4781-4793, (2024).

[22] S. Bhatnagar, G. Kumar, H. Mehdi, M. Kumar, "Optimization of FSW parameters for enhancing dissimilar joint strength of AA7050 and AA6061 using Response Surface Methodology (RSM)", *Mater. Today. Proc.*, (2023).

[23] A. Heidarzadeh, S. Mironov, R. Kaibyshev, G. Çam, A. Simar, A. Gerlich, F. Khodabakhshi, A. Mostafaei, D. P. Field, J. D. Robson, A. Deschamps and P. J. Withers, "Friction stir welding/processing of metals and alloys: A comprehensive review on microstructural evolution", *Prog. Mater. Sci.*, Vol. 117, 100752, (2021).

[24] A. S. Hamada, A. Järvenpää, M. M. Z. Ahmed, M. Jaskari, B. P. Wynne, D. A. Porter and L. P. Karjalainen, "Microstructural evolution and mechanical characterization of AA6082-T6 aluminum alloy friction stir welded joints", *Mat. Sci. Eng. A.*, Vol 642, pp. 366-376, (2015).

[25] Y. Zhao, W. Wen, Z. Wei, C. Wei, Y. Meng and M. Peng, "Microstructure and abnormal mechanical properties under the coupling effect of strain and temperature for friction-stir-welded joints of Al-Mg-Si alloy", *Mater. Today Commun.*, Vol. 39, 109273, (2024).

[26] J. Song, Y. Sun, W. Li, J. He, Z. Luo, C. He and X. Liu, "Microstructures, texture evolution and mechanical properties of dissimilar friction stir welded joints 5083-H111/6082-T6 with different welding speeds. *Mater. Today Commun.*, Vol. 48, 113480, (2025).

[27] V. Msomi, S. N. Mabuwa and A. Merdji, "Correlation between heat input and mechanical properties of submerged friction stir processed TIG- welded AA8011/AA6082 dissimilar joint: sampling aspect", *Pak. J. Engg. Appl. Sci.*, Vol. 30, pp. 23-33, (2022).

[28] A. Mirowska, M. Szkodo, Ł. Pawłowski, D. Moszczyńska and J. Mizera, "Influence of friction stir welding parameters on mechanical and electrochemical performance of EN AW-6082-T651 alloy butt joints", *Arch. Civ. Mech. Eng.*, 25, 290, (2025).

[29] N. Manuel, D. Beltrão, I. Galvão, R. M. Leal, J. D. Costa and A. Loureiro, "Influence of tool geometry and process parameters on torque, temperature, and quality of friction stir welds in dissimilar Al alloys", *Materials.*, Vol. 14, No. 20, 6020, (2021).

[30] C. Rathinasuriyan, M. Puviyarasan, R. Sankar and V. Selvakumar, "Effect of process parameters on weld geometry and mechanical properties in friction stir welding of AA2024 and AA7075 alloys", *J. Alloys Metall. Syst.*, Vol. 7, 100091, (2024).

[31] J. Yadav, N. Gangil, A. N. Siddiquee, M. E. A. Mohsin, K. Alnamasi, S. Q. Moinuddin, M. F. Khan and S. Maheshwari, "Effect of tool pin profiles on defects formation during friction stir welding of AA 6082-T6 straight-pipes-butt-weld joints", *J. Mater. Res. Technol.*, Vol. 36, pp. 1645-1657, (2025).

[32] M. Simoncini, A. Costa, S. Fichera and A. Forcellese, "Experimental analysis and optimization to maximize ultimate tensile strength and ultimate elongation of

friction stir welded AA6082 aluminum alloy", *Metals.*, Vol. 11, No. 1, 69, (2021).
[33] M. M. Z. Ahmed, B. Alzahrani, A. Bakkar, M. M. El-Sayed Seleman, A. Alamry and A. A. El-Aty, "Friction stir spot welding of AA6082-T6 alloy sheets with keyhole refilling using similar consumable rod material: mechanical performance and microstructure analysis", *Crystals.*, Vol. 15, No. 9, 751, (2025).
[34] K. Ramakanth, P. Y. Babu, G. V. Jagadeesh, S. Dey and G. T. N. Veerendra, "Prediction and optimization of process parameters of friction stir welded aluminum 6063 alloy", *J. Alloy Compd.*, Vol. 8, 100105, (2025).
[35] H. Wang, D. He, Y. Wu and S. Xu, "Real-time welding condition monitoring by roughness information extracted from surface images", *Measurement.*, Vol. 191, 110833, (2022).
[36] G. D. Bella, C. Borsellino, M. Chairi, D. Campanella and G. Buffa, "Effect of rotational speed on mechanical properties of AA5083/AA6082 friction stir welded T-joints for naval applications", *Metals.*, Vol. 14, No. 12, 1410, (2024).
[37] J. W. Choi, R. Hino, K. Ushioda, H. Fujii and S. J. Lee, "Critical review of solid-state welding for Al alloys with high joint efficiency: friction stir welding (FSW) vs. linear friction welding (LFW)", *Met. Mater. Int.*, (2025).
[38] C. Mohamed, Z. Samir, B. Benattou, M. Dahmane and G. Mehdi, "Influence of friction stir welding on microstructure and fatigue life of 6082-T6 aluminum alloy", *Int. J. Adv. Manuf. Technol.*, (2025).
[39] A. Tamadon, D. J. Pons and D. Clucas, "EBSD characterization of bobbin friction stir welding of AA6082-T6 aluminium alloy", *Adv. Mater. Sci.*, Vol. 20, No. 4, pp. 49-74, (2020).
[40] Y. S. Khan, M. H. Abidi, W. Malik, N. F. Lone, M. K. Aboudaif and M. K. Mohammed, "Effect of traverse speed variation on microstructural properties and corrosion behavior of friction stir welded WE43 Mg alloy joints", *Materials.*, Vol. 16, No. 14, 4902, (2023).
[41] C. Yu, H. Zhang, Y. Zhang, J. Zou, C. Guo, H.He, G. Xu, B. Li and J. Cui, "Influence of Mo on the dynamic recrystallization behavior of Al–Cu–Mg–Ag alloy. *J. Mater. Res. Technol.*, Vol 20, pp. 1437-1454, (2022).
[42] I. G. Papantoniou, P. Karmiris-Obratański, B. Leszczyńska-Madej and D. E. Manolakos, "Investigating the impact of friction stir processing on the hydrogen embrittlement in AA6082-T6 heat-treatable aluminum alloy", *Met. Mater. Int.* Vol. 30, pp. 2668-2684, (2024).
[43] F. F. Mustafa and S. R. Daham, "Investigation of process parameters for T-joint aluminum alloy 6061-T6 with nanocomposites material friction stir welding based on the Taguchi method", *J.Comput. Appl. Res. Mech. Eng.* Vol. 11. No. 1, pp. 101-111, (2021).

Copyrights ©2026 The author(s). This is an open access article distributed under the terms of the Creative Commons Attribution (CC BY 4.0), which permits unrestricted use, distribution, and reproduction in any medium, as long as the original authors and source are cited. No permission is required from the authors or the publishers.



How to cite this paper:

Worapong Boonchouytan, Watthanaphon Cheewawuttipong and Prapas Muangjunburee, " Influence of friction stir welding parameters on microstructural evolution and mechanical behavior of AA6082-T6 aluminum alloy", *J. Comput. Appl. Res. Mech. Eng.*, Vol. 15, No. 2, pp. 209-231, (2026).

DOI: 10.22061/jcarme.2026.12648.2745

URL: https://jcarme.sru.ac.ir/?_action=showPDF&article=2538